

1 **Seiche excitation in a highly stratified fjord of southern**
2 **Chile: the Reloncaví fjord.**

3

4

5 Manuel I. Castillo^{1,2*}, Oscar Pizarro^{2,3,4}, Nadin Ramírez^{2,4} and Mario Cáceres¹

6

7

8 [1]{Escuela de Biología Marina, Facultad de Ciencias del Mar y de Recursos Naturales,
9 Universidad de Valparaíso, Valparaíso, Chile.}

10 [2] {COPAS-Sur Austral, Universidad de Concepción, Concepción, Chile.}

11 [3] {Departamento de Geofísica, Universidad de Concepción, Concepción, Chile.}

12 [4] {Instituto Milenio de Oceanografía, Universidad de Concepción, Chile.}

13

14

15

16

17

18

19 *Correspondence to: manuel.castillo@uv.cl

20

21

22 **Abstract**

23

24 We describe a seiche process in a Chilean fjord, based on current, temperature and sealevel
25 data obtained from the Reloncavi fjord (41.6° S, 72.5° W) in southern Chile. We combined
26 four months of ADCP data with sealevel, temperature and wind time series to analyze the
27 dynamics of low-frequency (periods > 1 day) internal oscillations in the fjord. Additionally,
28 seasonal CTD data from 19 along-fjord stations were used to characterize the seasonality of
29 the density field. The density profiles were used to estimate the internal long-wave phase
30 speed (c) using two approximations: (1) a simple reduced gravity model (RGM) and (2) a
31 continuously stratified model (CSM). No major seasonal changes in c were observed using
32 either approximation (e.g., the CSM yielded $0.73 < c < 0.87 \text{ m s}^{-1}$ for mode 1). The natural
33 internal periods (T_N) were estimated using Merians's formula for a simple fjord-like basin
34 and the above phase speeds. Estimated values of T_N varied between 2.9 and 3.5 days and
35 were highly consistent with spectral peaks observed in the along-fjord currents and
36 temperature time series. We conclude that these oscillations were forced by the wind stress,
37 despite the moderate wind energy. Wind conditions at the end of winter gave us an excellent
38 opportunity to explore the damping process. The observed damping time (T_d) was relatively
39 long ($T_d = 9.1$ days).

40

41 **1 Introduction**

42

43 Internal seiche oscillation has long been known in closed basin geometries (e.g. Watson
44 1904; Wedderburn 1907; Wedderburn and Young 1915). The first detailed description
45 thereof was presented by Mortimer (1952). In these systems, wind is the main force affecting
46 the surface and isotherms (Wiegand and Chamberlain, 1987), which produces a set of
47 periodic oscillations and circulation cells throughout the water column that may contribute to
48 internal mixing of the basin (Thorpe 1974; Monismith 1985; Wiegand and Chamberlain
49 1987; Munnich et al. 1992; Mans et al. 2011; Simpson et al. 2011).

50

51 Although external (barotropic) seiches are ubiquitous in closed basin geometries (Munnich et
52 al. 1992), it is not theoretically evident that there are internal seiches (baroclinic) in a linearly
53 stratified fluid (Maas and Lam 1995). It is possible to find resonant basin modes only in

54 well-behaved geometries (Arneborg and Liljebladh, 2001a).. However, studies of lakes have
55 yielded good results using layered models (e.g. Lemmin 1987), normal-mode approximations
56 (e.g. Wiegand and Chamberlain 1987; Münnich et al. 1992) or numerical model simulations
57 (e.g. Goudsmit et al. 2002). In fact, internal seiches have been observed in semi-enclosed
58 systems such as fjords (e.g. Djurfeldt 1987; Pasmir and Stigebrandt 1997; Arneborg and
59 Liljebladh, 2001a) with complex geometries and where linear stratification is rarely
60 observed, and thus the only way to maintain consistency with the theory is that the
61 oscillation on the pycnocline dominates the internal seiche oscillation (Arneborg and
62 Liljebladh, 2001a). Early in the development of a seiche, its amplitude is related to the
63 forcing intensity, and the standing oscillation then becomes free and requires no additional
64 forcing. The frequencies are retained, but the amplitudes decays (damping) exponentially due
65 to friction until the system comes to rest (Rabinovich 2010). The development of seiche
66 oscillations depends of the forcing and damping mechanisms; with large damping, it is
67 impossible to observe a seiche, whereas small damping of a seiche allows for several
68 oscillations (Arneborg and Liljebladh, 2001a).

69

70 In fjords with shallow sills, the interaction between the sill and the barotropic tide generates
71 internal tides that are more energetic than other internal oscillations and are the focus of most
72 studies regarding mixing and internal oscillations based on internal tides (e.g. Stigebrandt
73 1980; Stigebrandt and Aure 1989; Inall and Rippeth 2002; Ross et al. 2014). In the case of
74 fjords with a deep sill and low tidal energy, the breaking of the internal seiche oscillations at
75 the boundaries could be an important contributor to the internal mixing, promoting the
76 spreading of properties within the fjord, particularly in deep waters (Stigebrandt and Aure
77 1989; Münnich et al. 1992; Arneborg and Liljebladh 2001b). Additionally, there are
78 evidences that vertical isopycnal displacements in fjords could be generated by similar
79 displacements outside the fjord (e.g. Svensen 1980; Djurfeldt 1987). These remotely
80 generated oscillations could enhance the mixing and ventilation in deep fjords.

81

82 There is still only limited understanding of the main oceanographic processes occurring in
83 the fjord region of southern Chile, although there has been local research during the previous
84 few decades. Since early studies of the hydrography by Pickard (1971), a systematic

85 measurement program in the fjord region has been maintained since 1995 (Palma and Silva
86 2008; Pantoja et al. 2011; Iriarte et al. 2014), although only a small number of studies have
87 focused on the physical dynamics. Most studies have been conducted over short time spans
88 (e.g. Cáceres et al. 2004; Valle-Levinson et al. 2007), and only a few studies have been based
89 on more than one month of data (e.g. Valle-Levinson and Blanco 2007; Letelier et al. 2011;
90 Castillo et al. 2012; Schneider et al. 2014), thereby limiting our understanding of sub-inertial
91 variability. In the Reloncavi fjord, time series of approximately 4 months have shown
92 evidence that 3-day oscillations of currents could be produced by internal seiche oscillations
93 (Castillo et al., 2012) but lack on the forcing to describe the forcing mechanism and the
94 seasonal modulation.

95

96 This study presents the first evidence of internal seiche oscillations in a fjord in southern
97 Chile. The objective of this study was to address the following questions: How do these
98 oscillations affect the temporal and spatial dynamics of currents and temperature? How are
99 these oscillations forced?

100

101 **2 Study area**

102

103 The Reloncavi fjord (41.5°S, 72.5°W) is the northern most fjords on the coast of Chile (Fig.
104 1). This "J" shaped fjord is 55 km long and has a width that varies from 3 km near the mouth
105 to 1 km near the head. There is a deep sill (~ 200 m depth) located 15 km inland although it
106 does not appear to be a barrier to the exchange of properties between the adjacent basins.
107 Based on bathymetric features and the coastline morphology, this fjord can be separated into
108 four sub-basins displaying the characteristics presented in Table 1 and figure 2.

109

110 The main river discharge is provided by the Puelo River (at the middle of the fjord), which
111 produces a mean annual discharge of $650 \text{ m}^3\text{s}^{-1}$. The Petrohue River (at the head of the fjord)
112 has an mean annual discharge of $255 \text{ m}^3\text{s}^{-1}$, and there are additional freshwater inputs of
113 minor importance compared with the Cochamo river (mean annual discharge of $20 \text{ m}^3\text{s}^{-1}$)
114 and Canutillar hydroelectrical plant (mean annual discharge $75.5 \text{ m}^3\text{s}^{-1}$) (Niemeyer and
115 Cereceda, 1984). The freshwater input to the fjord due to direct precipitation is only

116 approximately 2% of the main river discharge (León-Muñoz, 2013), and its contribution may
117 be in balance with evaporation (Castillo et al., 2016). The freshwater input creates a marked
118 along-fjord pycnocline that is deeper at the head (~8 m) and shallower at the mouth (~3 m)
119 (Fig. 2).

120

121 During the winter, the mean wind stress (τ) is low due to calms winds ($< 10^{-3} \text{ N m}^{-2}$). During
122 storm events in winter, τ can reach values as high as 0.4 N m^{-2} (winds of $> 10 \text{ m s}^{-1}$), and the
123 wind tends to blow out of the fjord, thereby reinforcing the upper outflow of brackish water.
124 In contrast, during the spring/summer, the winds exhibit a marked diurnal cycle, and τ can
125 reach values as high as those observed in the winter, whereas the wind blows landward, i.e.,
126 toward the fjord's head and against the upper flow. Tides in the Reloncavi fjord are
127 predominantly semi-diurnal, and during spring tidal range never exceed 6 m, whereas the
128 neap tidal range is about 2 m. The tidal current is relatively weak in the upper layer, which is
129 dominated by gravitational circulation (Valle-Levinson et al., 2007; Montero et al., 2011;
130 Castillo et al. 2012).

131

132 **3 Data and Methods**

133

134 **3.1 Field Observations**

135

136 Current measurements were obtained using Teledyne RD Instruments Acoustic Doppler
137 Currentmeter Profilers (ADCPs) in three subsurface mooring systems. These subsurface
138 systems were located near the fjord mouth, near the Puelo River and between the Cochamo
139 and Petrohue Rivers (Fig. 1). The longest time series spanned the period of August through
140 November 2008 (Fig. 1 and Table 1). At the mouth, two upper-looking ADCPs were
141 positioned at nominal depths of 10 m (300 kHz) and 450 m (75 kHz). The Puelo mooring
142 held two ADCPs, one facing-up at a depth of 30 m (600 kHz) and one facing downward at a
143 depth of 35 m (300 kHz). The Cochamo mooring held one facing-up ADCP at a depth of 11
144 m (300 kHz). Note that due to the large tidal range, the depths of the ADCPs significantly
145 changed with the tides. These effects — along with small vertical deviations of the ADCPs
146 related to the line movements — were corrected using the ADCPs pressure sensors, and all
147 of the bin depths were referenced to the water surface level. The mooring systems were

148 designed to obtain the best vertical resolution available with emphasis on the upper layer.
149 The ADCP cell sizes were 0.5 m (600 kHz), 1 m (300 kHz) and 4 m (75 kHz), and the data-
150 acquisition time intervals were 10 minutes in most of the ADCPs, with the exception of the
151 deepest ADCP, which was set to acquire data at an interval of 20 minutes. All the ADCPs
152 configurations maintain a standard deviation $< 2 \text{ cm s}^{-1}$ (details in supporting information
153 S2).

154

155 The morphology of the fjord exhibits a sharp bend in the middle, and thus the x and y -
156 components of the currents were rotated to the local orientation of the along-fjord axis (Fig.
157 1 and Table 1). A right-handed coordinate system with a positive-up z -axis and an along-
158 fjord y -axis (positive toward the fjord head) was used. Consequently, the cross-fjord x -
159 component was positive toward the south (east) near the fjord mouth (head). To assess the
160 contribution of the tides to the currents, the amplitudes and phases of several tidal
161 components were calculated at all of the moored ADCPs using a standard harmonic analysis
162 from Pawlowicz et al. (2002).

163

164 The vertical structure of the temperature was obtained from Onset HOB0-U22 temperature
165 sensors installed in three mooring systems along the fjord (Fig. 1). These moorings held
166 surface buoys supporting the thermistor chains with an anchor located at a 25 m depth to
167 maintain their nominal depths (0, 1, 2, 3, 4, 5, 7, 9, 11, 13, 15 and 20 m) from the surface
168 independent of tidal fluctuations. Temperature data were collected every 10 minutes at all
169 locations.

170

171 A Davis Vantage Pro2 meteorological station was installed south of the Puelo River (see Fig.
172 1). This station held sensors for measuring the wind direction and velocity, solar radiation,
173 rain, and air temperature. The wind magnitude and direction sensors were installed 10 m
174 above sealevel and were set to collect data every 10 minutes from 12 June 2008 to 30 March
175 2011. Gaps in the time series represented only 0.04% of the total data. The wind stress (τ)
176 was calculated using a drag coefficient dependent on the magnitude (see Large and Pond,
177 1981) and a constant air density of 1.2 kg m^{-3} .

178

179 The salinity and temperature profiles were obtained seasonally using a CTD SeaBird SBE 25
180 at 19 stations in the along-fjord transect shown on Figure 1. The data were processed
181 following the standard protocol suggested by the manufacturer and were averaged in vertical
182 intervals of 0.5 m. Due to large salinity changes in the upper layer, the instrument pump was
183 set to a time interval of 1 minute. After the start of the pumping, the instrument was
184 maintained near the surface until the sensors stabilization. Then, the CTD was lowered to the
185 maximum depth of the station (Table 2). The along-fjord transects typically required 12 to 24
186 hours to complete, depending on local weather conditions. Due to technical limitations, the
187 winter transect was performed to a maximum depth of 50 m.

188

189 The sealevel was recorded every 10 minutes using two pressure sensors moored over the
190 seabed. At Cochamo, the pressure sensor was an Onset HOBO-U20, whereas a SeaBird
191 wave-tide gauge SBE-26 was installed near the fjord's mouth (Fig. 1). Subsurface pressure
192 data were corrected for air pressure and converted to an adjusted sealevel.

193

194 Discharge data were provided by Dirección General de Aguas, Chile (Dirección General de
195 Aguas, 2016). These data are regularly collected at a station located 12 km upstream of the
196 Puelo River's mouth (Fig. 1). The time series extended from January 2003 to December
197 2011, and data gaps represented only 2% of the total.

198

199 **3.2 Time series analysis**

200

201 Previous findings (Castillo et al., 2012) have shown an important oscillation with a period of
202 approximately 3 days (72 h). To focus the study on these perturbations, we used a cosine-
203 Lanczos band-pass filter with half amplitudes at 60 h and 100 h (see results for the
204 justification of the selected band). As part of the results, the band-passed time series of the
205 current and temperature data are shown (COPAS-SUR Austral, 2012).

206

207 Spectral analyses of the current, wind stress, sealevel and temperature time series were
208 performed using Welch's modified average periodograms (Emery and Thomson 1998). To
209 achieve statistical reliability of the spectral estimations, each time series was divided into
210 non-overlapping segments to generate spectral estimates. In the case of the current time

211 series, the spectra were (additionally) averaged among depth layers to obtain 12, 24 and 48
 212 degrees of freedom, depending on the frequency (see Fig. 3). In addition, to evaluate the
 213 consistency of the periodicity between the time series, we calculate a Morlet cross-wavelet
 214 analysis following wavelet methods explained by (Torrence and Compo, 1998) and (Grinsted
 215 et al., 2004).

216

217 The phase velocity (c) was estimated using two models that took into account the fjord
 218 stratification: (1) a simple reduced-gravity model (RGM) and (2) a continuously stratified
 219 model (CSM).

220

221 The reduced-gravity model was developed using the typical density profiles in each sub-
 222 basin. Here, the base of the upper layer was estimated from the pycnocline depth (Fig. 2),
 223 which in the Reloncavi fjord is well represented by the depth of the 24 isohaline (h_I)
 224 (Castillo et al., 2016), considering that h_I is the pycnocline depth and H is the deepest CTD
 225 cast (mostly near to the sub-basins maximum depths). The mean density of the upper layer (ρ_1)
 226 was estimated from depths between the surface to h_I , whereas the mean density for the
 227 deep layer (ρ_2) was estimated for depths between h_I and H . These estimations were made
 228 for each sub-basins, and seasons (Table 2).

229

230 Using both densities, ρ_1 and ρ_2 , the reduced gravity ($g' = g(\rho_2 - \rho_1) / \rho_2$) was obtained,
 231 here g is the acceleration of gravity. The internal phase velocity of each sub-basin,

232 $c_i = (g' h_{Ii})^{1/2}$, where $i = 1$ to 4 and h_{Ii} represents the mean depth of the upper layer in the
 233 sub-basin “ i ” was used to estimate the effective phase speed in the entire fjord (eq. 1),

234
$$T = \frac{L}{c} = \sum_{i=1}^n \frac{L_i}{c_i} \quad (1)$$

235 where L_i is the i sub-basin length and L is the fjord length. This takes into account the
 236 changes of depth and lengths of fjord’s sub-basins.

237

238 The continuously stratified model (CSM) was developed using the normal mode analysis,
 239 which introduced the stratification as $N^2 = -(g / \rho)(\partial\rho / \partial z)$, which is the buoyancy
 240 frequency, in the Sturm-Liouville expression

$$241 \quad \frac{d}{dz} \left(\frac{1}{N^2} \frac{d\psi_n}{dz} \right) + \frac{1}{c_n^2} \psi_n = 0 \quad (2)$$

242 where $\psi_n(z)$ is the vertical structure of the horizontal velocity for the mode n . Here c_n
 243 represents the n mode speed (see Gill, 1982) and differs significantly from phase speed if
 244 rotation plays a role (van der Lee and Umlauf, 2011).

245

246 Independent of the model used to obtain the phase speed (RGM or CSM), the natural
 247 oscillation period (T_N) was determined using Merian's formula for a semi-enclosed basin, as
 248 suggested by Ravinovich (2010), $T_N = 4 T$.

249

250 The modal decomposition was used to obtain the contribution of each mode in the currents
 251 variability (e.g. Emery and Thomson, 1998; Gill, 1982; van der Lee and Umlauf, 2011). The
 252 along- and cross-fjord band-pass currents $[u_{bp}, v_{bp}]$ could be described by the vertical modes
 253 by (3),

$$254 \quad [u_{bp}, v_{bp}](z, t) = \sum_{n=1}^{\infty} [u_{pj}, v_{pj}](t) \psi_n(z) \quad (3)$$

255

256 The along- and cross-fjord currents projected (u_{pj}, v_{pj}) on the vertical modal structure (ψ_n)
 was obtained by eq. (4),

$$257 \quad [u_{pj}, v_{pj}](t) = \frac{1}{H} \int_{-H}^0 [u_{bp}, v_{bp}](z, t) \psi_n(z) dz \quad (4)$$

258

259 **4. Results**

260

261 **4.1 Density structure**

262 As a result of abundant freshwater input to the fjord, there were marked differences in
263 density between the upper and lower layers along the fjord and small changes in stratification
264 among seasons, particularly near the mouth of the fjord (Fig. 2). One important characteristic
265 of the upper layer is its high and persistent stratification from the surface to the base of the
266 pycnocline (Fig. 2). Along the fjord, the pycnocline depth exhibited clear deepening from 2.3
267 ± 0.1 m at the mouth to 6.1 ± 0.3 m near the head. The pycnocline depth exhibited greater
268 seasonal variability near the head of the fjord (Fig. 2).

269

270 **4.2 Winds, sealevel and freshwater discharge**

271

272 The along-fjord wind stress (τ) displayed two patterns during the transition from winter to
273 spring. During the winter, τ was generally out of the fjord ($-0.4 \pm 3 \times 10^{-2}$ N m⁻²) and
274 displayed oscillations with a period longer than 1 day. There were also strong events (> 0.2
275 N m⁻²) during the first half of August 2008 that could be associated with the end of winter
276 storms in the region. This winter pattern drastically changed during the early spring (first
277 week of September 2008) and was maintained throughout the rest of the season. Changes
278 were evident in a marked daily cycle and in switches from down- to up-fjord (average of 1.6
279 $\pm 3 \times 10^{-2}$ N m⁻²), against the upper layer outflow (Fig. 3a).

280

281 The sealevel was measured at the mouth and near Cochamo (Fig. 1). At both stations, the
282 form factor was 0.12, which indicates that semi-diurnal tides dominate in the region. In fact,
283 the M_2 amplitude was 1.89 ± 0.06 m at the mouth and 1.91 ± 0.06 m near Cochamo. The
284 mouth-to-head phase difference in this harmonic was negative (-2.4°), indicating propagation
285 toward the head with a lag of approximately 5 minutes. The maximum tidal range during
286 spring tides was approximately 6 m and less than 1 m during neap tides (Fig. 3b). Similar
287 ranges have been observed outside the fjord in the Reloncavi sound (Aiken, 2008).

288

289 Discharge was greatest (approximately $1413 \text{ m}^3 \text{ s}^{-1}$) at the end of August 2008 (winter) and
290 lowers (approximately $459 \text{ m}^3 \text{ s}^{-1}$) at the end of October (spring). In the winter, the historical
291 mean of $650 \text{ m}^3 \text{ s}^{-1}$ (Niemeyer and Cereceda 1984; Leon et al 2013) was exceeded 86% of
292 the time, whereas during the spring, this exceedance occurred only 18% of the time. In fact,
293 only a small variability around the mean was observed during the spring (Fig. 3c).

294

295 **4.3 Along-fjord currents**

296

297 The along-fjord currents were one order of magnitude larger than the cross-fjord currents (in
298 this study we focused on the along-fjord component). At the three measurements sites at
299 Cochamo (Fig. 3d), Puelo (Fig. 3e) and the mouth (Fig. 3f), the along-fjord currents
300 displayed certain common features: (1) semi-diurnal oscillations attributed to tidal effect, (2)
301 a two layered structure with persistent outflow above the pycnocline and an intermittent
302 lower inflow layer beneath, and (3) several low-frequency (period > 1 day) oscillations were
303 present in the time series.

304

305 Currents in the upper outflow layer displayed a mean velocity of 66 cm s^{-1} at the mouth and
306 45 cm s^{-1} at Cochamo, indicating that the outflow increased through the mouth. Additionally,
307 the upper layer was deeper at Cochamo (Fig. 3d) than at the mouth (Fig. 3f), which is
308 consistent with the along-fjord pycnocline depth (Fig. 2). Below the upper layer, a sub-
309 surface layer displayed intermittent inflow (see Fig. 3d, 3e and 3f) with a maximum ($> 20 \text{ cm}$
310 s^{-1}) centered at the $\sim 6 \text{ m}$ depth.

311

312 This two-layered pattern was clearly observed in the upper 10-15 m and is consistent with a
313 gravitational circulation due to the along-fjord pressure gradient. This pressure gradient is
314 also consistent with the observed along-fjord pycnocline tilt (Fig. 2). At depths $> 20 \text{ m}$, the
315 along-fjord currents at Puelo and at the mouth exhibited an important influence ($> 40\%$ of
316 the variability) of a semi-diurnal component of the tide. In addition, in this layer, low-
317 frequency (periods > 7 days) oscillations suggest a bottom-to-surface propagation that was
318 more intense from the end of August to the beginning of September during a period of high

319 discharge ($> 650 \text{ m}^3 \text{ s}^{-1}$). This layer on average exhibited a weak outflow ($\sim 1 \text{ cm s}^{-1}$) at the
320 mouth, which in turn implies a 3-layer pattern of the residual flow near the mouth.

321

322 **4.4 Spectral characteristics of currents, temperature, sealevel and winds**

323

324 To obtain better statistic reliability, the spectra of the along-fjord currents were depth-
325 averaged. The upper layer was defined until the pycnocline depth ($z \leq h_l$), whereas the deep
326 layer contains $z > h_l$ (Fig. 4).

327

328 All of the spectra displayed an energetic peak at the semi-diurnal frequency (M_2), and this
329 peak was greater in the deep layer (Fig. 4). In the diurnal band, the spectra at Puelo and at the
330 mouth presented a clear (and highly energetic) peak in the surface layers. This diurnal peak
331 is likely due to the influence of wind stress (see Fig. S1), which displayed a marked diurnal
332 cycle during the late winter (end of August) and spring (Fig. 3a). An important peak (10^4 cm^2
333 $\text{s}^{-2} \text{ cph}^{-1}$) was observed only at Cochamo in the 6 hour band (M_4), suggesting an increase in
334 the importance of non-linear interaction between M_2 and the bathymetry in this sub-basin.
335 The spectra in the upper layer displayed an important accumulation of energy in the band
336 centered on the 3days period. The band was wider (between 2 and 7 days) at the mouth and
337 Puelo and narrower (between 1.5 and 4 days) at Cochamo. At the mouth, the maximum
338 spectral density was in the 3 days band ($> 10^5 \text{ cm}^2 \text{ s}^{-2} \text{ cph}^{-1}$) and was one order greater than
339 the maximum spectral density observed at Cochamo ($\sim 10^4 \text{ cm}^2 \text{ s}^{-2} \text{ cph}^{-1}$). Another important
340 accumulation of energy in the along-fjord currents was centered on the 15 days period. One
341 characteristic of the 15 days band is the influence on the entire water column at Puelo and the
342 mouth (Fig. 4).

343

344 The sealevels at Cochamo (η_c) and at the mouth (η_m) were similar at frequencies less than
345 0.165 cph (periods longer than 6 h). The spectra displayed an important accumulation in the
346 synoptic band (10 days). Both locations exhibited the same energy at the diurnal (K_1)
347 semidiurnal (M_2) frequencies, although M_2 was clearly the dominant harmonic in the fjord.
348 The spectral energy was one order of magnitude higher than the diurnal (K_1) harmonics and
349 three orders of magnitude higher than the quarter-diurnal (M_4) harmonics. The spectra

350 exhibited no accumulation of energy in the 3days band, although at high frequencies (> 0.5
351 cph), an important accumulation of energy was observed in the 1.3h band (between 1.16 h
352 and 1.56 h) at η_C (Fig. 4).

353

354 The wind stress (τ) indicated that the along-fjord wind stress was significantly higher than
355 the cross-fjord component. The spectra displayed a marked peak (particularly in the along-
356 fjord component) in the diurnal band, which is likely due to the sea-breeze phenomenon.

357 Another interesting feature of the spectrum was the peak in the semi-diurnal frequency,
358 which was observed in both components. At longer periods (> 1 day), the along-fjord wind
359 stress displayed an important but not statistically significant peak at 2.8 days, which is highly
360 consistent with the currents (Fig. 4).

361

362 **4.5 Seasonality of the internal oscillations**

363

364 The density structure on the fjord does not show an upper mixing layer along the seasons;
365 indeed a continuously stratified upper layer is present along the seasons (Fig. 5). The along-
366 fjord mean of the pycnocline depth (h_I), which was estimated based on salinity/density
367 gradient, was used to estimate the internal phase velocity (c) and the internal period (T_N).

368 Seasonally, h_I does not change significantly during winter, spring and summer (between 4.6
369 and 4.8 m) but was shallower during autumn (~ 4.1 m) (Table 2). In addition, the density
370 structure showed a condition of continuous stratification in the upper layer along the seasons
371 (Fig. 5).

372

373 In the case of the RGM approximation, internal phase velocities (c) were highest during
374 spring and summer (> 0.83 m s $^{-1}$) whereas in winter and autumn the intensities were < 0.76
375 m s $^{-1}$, thus we obtain internal periods between 2.9 and 3.4 days (70 and 82 hours) (Table 2).

376

377 The horizontal velocity structure (ψ_n) profile of the first 3 internal modes obtained from the
378 CSM, showed high consistency along the fjord (in each sub-basin) and through the seasons
379 (Fig 5). The mode 1 was highly baroclinic changing of sign nearly of 10 m (sub-basin I) and
380 15 m (sub-basin IV). In the case of mode 2 and 3, relatively high variability along the

381 seasons was observed specially at the sub-basins I and IV above of 20 m depth. For depths >
382 30 m (not shown) the internal modes do not show significant variability (Fig. 5). The modal
383 speeds for the first 3 modes described above were relatively high during spring and summer
384 (c_I was $> 0.84 \text{ m s}^{-1}$) and lower during winter and autumn (here c_I was $< 0.77 \text{ m s}^{-1}$). These
385 results were highly consistent with the internal speeds obtained by RGM (Table 2).

386

387 As the internal speeds (c), the natural internal period (T_N) obtained by RGM with the mode 1
388 of CSM were highly consistent. For comparison, we take into account T_N obtained from the
389 mode 1 of the CSM which ranged between 2.9 days (spring) and 3.5 days (winter). The
390 estimations of T_N with RGM showed speeds between 2.9 days (spring) and 3.4 days (winter
391 and autumn), indicating that oscillations between these periods are dominated by mode 1
392 internal seiche oscillation.

393

394 To focus on these internal seiche oscillations, we filtered the along-fjord currents with a 70h
395 to 90h cosine-Lanczos band-pass filter. Additionally, mode 1 of the internal seiche was
396 associated with the pycnocline depth, which is restricted to the upper 8 m (Fig. 2). Therefore,
397 we describe the along-fjord currents in the upper 10 m (Fig. 6).

398

399 Vertical pattern at the three locations shows inflow/outflow intermittence along the whole
400 time series, also mostly of these along-fjord structures seems to develop an inclination which
401 suggest the baroclinic nature of this pattern. The band-pass along-fjord currents were intense
402 at the mouth ($> 15 \text{ cm s}^{-1}$) but diminish toward the head. Intense perturbations oscillations
403 were observed near the surface between 10 and 20 August 2008 at the mouth and Cochamo,
404 internal intensification (between 4 m and 10 m depths) of the inflow/outflow pattern was
405 clear at Puelo and Cochamo at the ends of September. To confirm whether the nature of the
406 along-fjord currents pattern was baroclinic or barotropic we used $\psi_n(z)$ to project the band-
407 pass currents (eq. 3 and 4), similar to van der Lee and Umlauf (2011).

408

409 The adjustment between the 3 days band-pass and the projected along-fjord currents at the
410 mouth it is showed on Fig. 7. Here, using only the first three modes was possible of explain
411 more than 70% of the band-pass variability, changes in the outflow/inflow were highly

412 consistent and the intensifications at the surface was clearly showed by the projected modes.
413 In addition, the vertical structures of the outflow/inflow were well defined by the projections.
414 To make an approximation of the relative importance of the currents variability we estimated
415 kinetic energy ($K_E = (u^2 + v^2) / 2$) of i) the projected modes 1-3, ii) the 3 days band-pass
416 and iii) the semi-diurnal (12h) + diurnal band pass (1d) along-fjord currents at the mouth.

417

418 The vertical averaged K_E shows that 3 days band-pass was higher than the other the
419 components (modes 1-3), maximum was observed at between August 9 to 18 (Fig. 7), dates
420 which were consistent with the wind-stress intensification (Fig. 3a). During this period, the
421 modal K_E was one third of the 3 days band-pass kinetic energy, this ratio enhanced during
422 September, were the projected currents were c.a. 50% of the 3 days band-pass currents. The
423 relatively importance of the tides at the mouth was estimated summing the K_E of the diurnal
424 and semi-diurnal currents. In terms of energy, the K_E contribution of tides was similar to the
425 modal currents (Fig. 7).

426

427 Along-currents were highly coherent at 3 days band which is the period of the first mode of
428 the internal seiche (Table 2). To describe the variability of this high coherence along the
429 time, we selected 3 m depth ADCP bins (on the upper layer) from the mouth, Puelo and
430 Cochamo to make a Morlet cross-wavelet analysis and to estimate the squared coherence
431 (only refer as coherence hereafter) and phase spectrums for the relations mouth/Puelo (MP)
432 (Fig. 8b, 8c) and Puelo/Cochamo (PC) (Fig. 8d, 8e). Both relations showed high coherence in
433 the semi-diurnal and diurnal band especially during spring-tides.

434

435 A low coherence (< 0.6) was observed during the opposite winds (Fig. 8a and 8b). Similarly,
436 the coherence for the PC relation was high along the 3 days band except during the change of
437 the wind direction described above (Fig. 8d). The associated phase spectra (only the
438 significant coherence) at the 3 days band was $\sim 0^\circ$ indicating that the oscillation is in phase
439 along the fjord (Fig. 8c and 8e).

440

441 At the beginning of the time series, intense fluctuations were observed at Cochamo and at the
442 mouth (Fig. 6). To explore their relationship with the wind forcing, a detailed view of the

443 period between 8 and 31 August 2008, is presented in Fig. 9. During this period, the along-
444 fjord wind stress (not filtered) displayed three different states: (a) strong ($> 0.2 \text{ N m}^{-2}$) up to
445 the fjord winds, (b) weak ($< 0.1 \text{ N m}^{-2}$) or nearly calm winds and (c) moderate ($\sim - 0.1 \text{ N m}^{-2}$)
446 down to the fjord winds. During (c), the winds displayed an apparent diurnal cycle (e.g.,
447 Fig. 3a).

448

449 Although density is dominated by salinity, here we used temperature moorings to emphasize
450 that the internal oscillation reported here had an expression in other properties of the water
451 within the fjord. In addition, the band-pass temperature time series and the along-fjord
452 currents shows consistent oscillations pattern (Fig. 9). During (a), the upper outflows
453 weakened due to the opposing winds at the surface. This change reached depths consistent
454 with the pycnocline (Fig. 2), caused a disruption and subsequently forced the internal
455 oscillations observed in the currents and temperature fields (Fig. 9). Here, intense
456 perturbations were observed that weakened the surface outflow and introduced the colder
457 water of the upper layer to depths $> 2 \text{ m}$ at Cochamo and Puelo. During (b), the upper
458 outflow displayed minimum perturbations in both the currents and temperature. In (c),
459 perturbations in the currents and temperature were evident at Cochamo and at the mouth with
460 no major oscillations at Puelo (Fig. 9). In addition, 3 days band-pass vertical velocities (w)
461 were included as arrows on the contours of the along-fjord currents in Fig. 9. The maximum
462 w were 1 cm/s at the mouth, outflow (inflow) was related with downward (upward)
463 circulation in the entire fjord. This imply that the oscillation observed on the along-fjord
464 currents also was consistent with the vertical velocities pattern.

465

466

467 **5 Discussion**

468

469 We used data from one of the most extensive study ever conducted in a Chilean fjord. The
470 data included currents (ADCPs) and temperatures from moored instruments, seasonal CTD
471 information and times series of winds and sealevel to study the dynamics of the internal
472 seiche oscillations in the Reloncavi fjord.

473

474 In fjords with shallow sills such as the Gullmar fjord in Sweden (Arneborg and Liljebladh,
475 2001a), the Knight Inlet in Canada (Farmer and Freeland, 1983) and the Aysen fjord in Chile
476 (Cáceres et al., 2002), internal tide oscillations may play a key role in the internal mixing
477 (e.g. Stigebrandt 1976; Farmer and Smith 1980). In lakes, large internal seiche oscillations
478 significantly contribute to the mixing of the entire basin (Cossu and Wells, 2013), and these
479 oscillations could also be important in fjords where the relative importance of internal tides
480 may be less than the internal seiche oscillations (Arneborg and Liljebladh, 2001b).

481

482 In this study, we demonstrate the presence (and persistence) of seiches in a Chilean fjord
483 based on the sealevel slope (barotropic seiche), currents and temperatures (internal seiche).
484 We also studied the main processes forcing the natural oscillation of the pycnocline.

485

486 At high frequencies, the tidal spectrum (Fig. 4) displayed a clear accumulation of energy
487 centered at a period of 1.3 h. This frequency is not related to any tidal harmonic interactions
488 (Pawlowicz et al., 2002), and the shape of the spectrum (it is not a peak) suggests resonance
489 in this frequency band. We explored the effect of the natural oscillation of the basin in this
490 pattern using the barotropic phase velocity (c) for a shallow water wave $c = (gh)^{1/2}$, where h
491 is the mean depth of the fjord. If one assumes a mean fjord depth of $h = 250$ m (Table 1),
492 then $c = 49.5$ m s⁻¹, and the natural period $T_N = 4L c^{-1} = 1.24$ h. This period is lower than the
493 observed period in Fig. 5 (1.3 h) because the mean depth takes into account the entire fjord
494 bottom profile (Fig. 1), and thus the effective depth (up to Cochamo) was 233 m and it is
495 closer to the 226 m necessary to obtain the observed period in Fig. 5. Winds in the region are
496 moderate (see Fig. 3), but their intensity is sufficient to tilt the surface slope at Cochamo
497 (Castillo et al., 2012), and thus the surface of the fjord oscillates with the natural period of
498 the basin. Further evidence of this pattern is provided by the clear differences in amplitude of
499 the sealevel spectrum at Cochamo (near the fjord's head) and at the mouth. This association
500 is attributed to the dynamics of seiches in fjords, which tend to produce a node at the mouth
501 and an anti-node at the head (Dyer, 1997). At the node, the sealevel amplitude must be zero,
502 whereas near the head, it must be a maximum. This pattern is highly consistent with the
503 observed spectra at 1.3 h (Fig. 5). Based on all of these results, we suggest that oscillations
504 close to 1.3 h will resonate with the natural period along the fjord.

505

506 Daily winds were highly coherent with surface along-fjord currents, especially on the
507 brackish water layer (S1). During the spring, daily periodicity of winds was strong (Castillo
508 et al., 2016) with intensities capable of perturbing the pycnocline and to induce the internal
509 seiching process.

510

511 The surface slope indicates that the sealevel at Cochamo was 0.07 m higher than at the
512 mouth, and this value can be taken as the amplitude of the surface seiche. According to the
513 RGM, the pycnocline deviation (η_l) is related to the surface elevation (η_0) in the form
514 $\eta_l = -(\rho / \Delta\rho) \eta_0$, which implies that for a mean surface perturbation of 0.07 m and a
515 typical $\Delta\rho$ of 15 kg m^{-3} , we obtain a mean η_l of -4.8 m. This finding indicates that the water
516 piles up at the head of the fjord, likely due to the predominant into the fjord winds in the
517 region (Fig. 3a) and produces a pycnocline deepening of about 5 m (Fig. 2).

518

519 At low frequencies (periods > 1 day), the along-fjord currents spectra displayed a marked
520 peak in energy centered at 3 days. To explore the origin of this variability, we analyzed the
521 density profiles along the fjord (Fig. 2) and applied two methods, the RGM and CSM. The
522 internal phase velocities (c) obtained from both methods were similar, and ranged between
523 0.73 m s^{-1} and 0.87 m s^{-1} (taking into account the mode 1 of CSM for comparison). The high
524 c value was obtained during the spring (November 2008), when the upper layer presented the
525 lowest densities of the seasons, likely due to high discharge ($> 1000 \text{ m}^3 \text{ s}^{-1}$). Remarkably, the
526 stratification is linked to the freshwater input despite no major observed changes in c (Fig.
527 6e-h). The high consistency between the CSM (mode 1) modal speeds and the phase speed
528 obtained by RGM suggest that rotation do not play a significant role on the along-fjord
529 dynamics of these oscillations (van der Lee and Umlauf, 2011). But cross-fjord, the
530 dynamics has been nearly geostrophic, especially at the fjord's mouth (Castillo et al., 2012).

531

532 For longer periods (> 10 days), there are evidences of baroclinic oscillations clearly observed
533 on the along-fjord time series (Fig. 3) and in the averaged spectra (Fig. 4). Recently, Ross et
534 al. (2015), described a similar periodicity on currents of a southern Patagonian fjord of Chile
535 associated to Baroclinic Annular variability, a regional feature on the air-pressure in the

536 region. This mechanism of generation for the 10 days oscillations on the Reloncavi fjord
537 needs to be verified on future studies.

538

539 The internal T_N of the entire fjord displayed periods between 2.9 and 3.5 days. These results
540 suggest that the accumulation of energy observed in the along-fjord currents are due to the
541 first mode of an internal seiche oscillation in the fjord. This result could be explained by the
542 presence of a node at the mouth, where the sealevel amplitude is minimum (Fig. 5) but the
543 currents are maxima (Figs. 3 and 6). This difference was also observed in the projected
544 currents (u_{pj} , v_{pj}) supporting the idea of the presence stationary wave along the fjord.
545 Additionally, the currents were highly coherent and in phase (Fig. 8) as we expected from a
546 basin-scale seiche wave like. As a way to estimate the contribution of the internal seiche to
547 the internal mixing the K_E was enhanced during the into the fjord winds (Figs. 3 and 7),
548 which were periods when the internal seiche band (3 days) was highly coherent along the
549 fjord (Fig. 8).

550

551 The winds exhibited high coherence with the along-fjord currents until the pycnocline
552 depths, at frequencies centered at 1 and 3 days (see Fig. S1). To study the extent to which the
553 wind stress perturbs the pycnocline, we used the Wedderburn number, which is given by the
554 equation $W = (h_1 / L) Ri$ (Thompson and Imberger, 1980; Monismith, 1986), where
555 $Ri = g'(h_1 / u_*^2)$ represents the bulk Richardson number, an index of the stability of the upper
556 layer (h_1). The frictional velocity (u_*) is obtained from the surface wind stress using the
557 equation $u_*^2 = \tau / \rho_0$, which results in the equation,

558
$$W = \frac{h_1^2 \Delta \rho g}{L \tau} \quad (5)$$

559

560 According to Thompson and Imberger (1980), this value indicates the effect of the wind
561 stress on local upwelling in a stratified fluid (i.e., perturbing the pycnocline). Under weak τ
562 conditions ($W \gg 1$), the wind energy is insufficient to tilt the interface. Under strong τ
563 conditions ($W \ll 1$), however, upwelling conditions dominate, there by tilting the interface,
564 which produces conditions favorable to forcing of the internal seiche. The critical conditions
565 ($W \sim 1$) indicate the beginning of upwelling (Thompson and Imberger, 1980; Stevens and

566 Imberger, 1996), although the ideal transition point occurs at $W = 0.5$ (Monismith, 1986). All
567 of these conditions were observed during the period of August 2008, as it is shown on Fig. 9.
568 During strong τ ($\sim 0.3 \text{ N m}^{-2}$) conditions, $W = 0.27$ produced intense perturbation of the
569 pycnocline (Fig. 9a). In contrast, during weak τ ($\sim 0.01 \text{ N m}^{-2}$) conditions, a value of $W = 8$
570 indicates that the wind was too weak to perturb the pycnocline, favoring a seiche damping
571 process (Fig. 9b). Transition conditions occurred when $\tau \sim 0.1 \text{ N m}^{-2}$ and $W = 0.8$, indicating
572 that the winds were strong enough to perturb the pycnocline and stop the damping process
573 (Fig. 9c).

574

575 **5.1 Internal seiche damping**

576

577 The wind stress changed from a state where τ was strong enough to actively disturb the
578 pycnocline ($W < 1$) to a period of nearly calm winds ($W > 1$) between the 16 and 24 August
579 2008 (Fig. 9). During this period, both the along-fjord currents and temperatures tended to
580 decay, which is clearly evident in the isolines of these properties at the three sites (Fig. 9).

581

582 To study the damping process in detail, we selected the time series of the along-fjord
583 currents at a depth of 3 m at Cochamo during the above period in August to span the period
584 of forcing, damping and re-enforcing of the internal oscillation.

585

586 Typically, any real oscillations undergo damping, which is given by the equation,

$$587 \quad x(t) = A e^{(-k t)} \cos(\omega t + \phi) \quad (7)$$

588 where t is time and A is the initial amplitude, k is the damping coefficient which has units of
589 $[\text{s}^{-1}]$, $\omega = 2\pi/T_N$ and ϕ is the phase. In the case studied here, $\phi = 0$, $A = 8 \text{ cms}^{-1}$, and $T_N = 2.5$
590 days, which was the internal period at Cochamo (Fig. 4). The best fit occurred when $k = 1/3$
591 (Fig. 10).

592

593 The time for the initial amplitude A to decay to $A \sim 0$ is the damping time (T_d). There was a
594 good fit (Fig. 10) between the observed current and the curve adjusted with the damping
595 effect. Here, $T_d = 9.1$ days, which is more than 3 times longer than the natural oscillation

596 (T_N); more precisely, $T_d = 3.6 T_N$ at this site. The observed internal oscillations of the
597 currents were not completely damped because the winds increased from nearly calm ($W > 1$)
598 to moderate conditions, which disturbed the pycnocline ($W \sim 1$) and induced the intense
599 oscillations during the spring (Fig. 6). In the spring, the winds displayed a marked diurnal
600 cycle that remained during the spring and summer (Castillo et al., 2012). This finding
601 suggests that the internal seiche (mode 1) process is active without damping because it is
602 forced daily (Fig. 3). Our findings indicated that the internal seiche process is an active
603 contributor for the mixing in the Reloncavi fjord, the magnitude of this contribution might be
604 similar as the tidal forcing. The maximum amplitude of the tidal currents on the Reloncavi
605 fjord is 10 cm s^{-1} (Valle-Levinson et al., 2007; Castillo et al., 2012), using the K_E to estimate
606 the maximum contribution of the tide obtain $5 \times 10^{-3} \text{ m}^2 \text{ s}^{-2}$ which is similar to the observed
607 K_E at the mouth (Fig. 7). One example of the dissipation of the energy through this process
608 was observed previous to 19 August 2008 (Fig. 10), on there the maximum currents were 0.7
609 m s^{-1} and through eq. 7, we obtain $K_E = 7 \times 10^{-3} \text{ m}^2 \text{ s}^{-2}$ great part of this energy might be
610 dissipated within the Reloncavi fjord on 9 days. Future studies should focus on evaluating
611 more precisely the available energy for the mixing process within the fjord and their effects
612 on other water properties such as the salinity, oxygen or nutrients.

613

614 **6 Conclusions**

615

616 The along-fjord seasonal density structure of the Reloncavi fjord showed small changes in
617 the stratification. The upper layer presents a persistent stratification from the surface to the
618 pycnocline base, the latter of which has a mean depth of 2 m near the mouth and 6 m near the
619 head of the fjord.

620

621 The along-fjord sealevel signal showed a 1.3 h energetic peak not related with any tidal
622 harmonics, additionally at this period the sealevel amplitude at the mouth was significantly
623 higher than the sealevel at the head of the fjord. This pattern was consistent with the presence
624 of a barotropic seiche on the Reloncavi fjord.

625

626 The local winds stress was able to perturb the along-fjord pycnocline and produce internal
627 seiche oscillations. The period centered on 3 days was consistent with the first baroclinic
628 oscillation mode. This mode explained 44% of the variability of the 3 days band. The
629 oscillation was highly coherent along the fjord and with a phase nearly to 0° , consistent with
630 a standing wave, like an internal seiche, within the Reloncavi fjord.

631

632 The internal seiche could be high contributor to the internal mixing within the fjord, in fact
633 the kinetic energy (K_E) associated to the internal seiche was similar to the maximum
634 contribution of the tides in the along-fjord currents. During winter, the internal oscillations
635 were present a relatively long period of time with nearly calm winds permit the estimation of
636 the damping time of the internal seiche which was of 9 days, otherwise during the spring
637 daily winds continuously forced the pycnocline.

638

639 **Data availability**

640

641 The installation of the moorings for measuring the current, temperature and sealevel in the
642 region was approved by the Chilean Navy through permit DS711. No specific permits were
643 required to install the meteorological station because the location is a publicly controlled site.
644 This study also did not involve any endangerment to species in the region. The authors
645 indicated that all data are available to download from a COPAS-SUR Austral website
646 (<http://www.reloncavi.udec.cl/>, last access 6 June 2016). The discharge data from the rivers
647 of Chile are available from the Dirección General del Aguas de Chile website
648 (<http://dgasatel.mop.cl/>, last access 1 July 2016). Also, all data sets can be requested from the
649 corresponding author (Manuel I. Castillo).

650

651 **Acknowledgements**

652 The authors thank the students (from Chile and Sweden) and technicians of the Physical
653 Oceanography group of the Universidad de Concepcion who collaborated in performing the
654 field measurements. This study is part of the COPAS-Sur Austral CONICYT PIA PFB31
655 and Centro de Investigación en Ecosistemas de la Patagonia by FIP2007-21. Manuel I.

656 Castillo was supported by CONICYT-PAI no. 791220005 and by FONDECYT no.
657 11160500.

658

659 **References**

660

661 Arneborg, L., and B. Liljebladh.: The internal seiches in Gullmar fjord part I -dynamics.
662 *Journal of Physical Oceanography* **31**: 2549-2566, 2001a.

663 Arneborg, L., and B. Liljebladh: The internal seiches in Gullmar fjord part II - contribution
664 to basin water mixing. *Journal of Physical Oceanography* **31**: 2567-2574, 2001b.

665 Cáceres, M., A. Valle-Levinson, H. Sepúlveda, and K. Holderied: Transverse variability of
666 flow and density in a Chilean fjord. *Continental Shelf Research* **22**: 1683–1698,
667 2002.

668 Castillo, M. I., O. Pizarro, U. Cifuentes, N. Ramirez, and L. Djurfeldt: Subtidal dynamics in
669 a deep fjord of southern Chile. *Continental Shelf Research* **49**: 73-89, 2012.

670 Castillo, M. I., U. Cifuentes, O. Pizarro, L. Djurfeldt, and M. Caceres: Seasonal hydrography
671 and surface outflow in a fjord with a deep sill: the Reloncaví fjord, Chile. *Ocean Sci.*
672 **12**: 533-544, 2016.

673 COPAS-Sur Austral: Oceanografía del fiordo Reloncaví, Universidad de Concepción,
674 available at: <http://www.reloncavi.udec.cl/>, last access 6 June 2016, 2012.

675 Cossu R, Wells MG. The Interaction of Large Amplitude Internal Seiches with a Shallow
676 Sloping Lakebed: Observations of Benthic Turbulence in Lake Simcoe, Ontario,
677 Canada, PLOS ONE doi: 10.1371/journal.pone.0057444, 2013.

678 Dirección General de Aguas: Datos hidrológicos en tiempo real, Chile, available at:
679 <http://dgasatel.mop.cl/>, last access 1 July 2016, 2016.

680 Djurfeldt, L.: On the response of the Fjord Gullmaren under ice cover, *J. of Geophys. Res.*,
681 **92**, 5157-5167, doi: 10.1029/JC092iC05p05157, 1987.

682 Dyer, K. R.: *Estuaries: A Physical Introduction*, John Wiley and Sons Inc, 140 pp., UK,
683 1997.

684 Emery, W. J., and Thomson, R. E.: *Data Analysis Methods in Physical Oceanography*, 634
685 pp., Elsevier, New York, USA, 1998.

686 Farmer, D. M., and Freeland, H. J.: The physical oceanography of Fjords. *Prog. in*
687 *Oceanogr.*, **12**, 147-194, doi: 10.1016/0079-6611(83)90004-6, 1983.

688 Farmer, D. M., and Smith, J.: Tidal interaction of stratified flow with a sill in Knight Inlet.
689 *Deep Sea Research Part A. Oceanographic Research Papers*, **27**, 239-254, doi:
690 10.1016/0198-0149(80)90015-1, 1980.

691 Gill, A.: *Atmosphere-Ocean Dynamics*, Academic Press, 662 pp., USA, 1982.

692 Goudsmit, G.-H., Burchard, H., Peeters, F. and Wüest, A.: Application of k- ϵ turbulence
693 models to enclosed basins: The role of internal seiches, *J. Geophys. Res.*, **107**, 3230,
694 doi: 10.1029/2001JC000954, 2002.

695 Grinsted, A., Moore, J. C., and Jevrejeva, S.: Application of the cross wavelet transform and
696 wavelet coherence to geophysical time series, *Nonlin. Processes Geophys.*, **11**, 561-
697 566, doi:10.5194/npg-11-561-2004, 2004.

698 Inall, M. E., and Rippeth, T. P.: Dissipation of Tidal Energy and Associated Mixing in a
699 Wide Fjord, *Environmental Fluid Mechanics*, **2**, 219-240, doi:
700 10.1023/A:1019846829875, 2002.

701 Iriarte, J. L., Pantoja, S., and Daneri, G.: Oceanographic Processes in Chilean Fjords of
702 Patagonia: from small to large-scale studies, *Prog. in Oceanogr.*, 129, 1-7, doi:
703 10.1016/j.pocean.2014.10.004 , 2014.
704

705 Large, W. G., and Pond, S.: Open-ocean momentum flux measurements in moderate to
706 strong winds, *J. Phys. Oceanogr.*, 11, 324-336, 1981.

707 Lemmin, U.: The structure and dynamics of internal waves in Baldeggersee, *Limnol.*
708 *Oceanogr.*, 32, 43-61, doi: 10.4319/lo.1987.32.1.0043, 1987.

709 León-Muñoz, J., Marcé, R., and Iriarte, J. L.: Influence of hydrological regime of an Andean
710 river on salinity, temperature and oxygen in a Patagonia fjord, Chile, *New Zeal. J.*
711 *Mar. Fresh.*, 47, 515–528, doi: 10.1080/00288330.2013.802700, 2013.

712 Letelier, J., Soto-Mardones, L., Salinas, S., Osuna, P., López, D., Sepúlveda, H. H., Pinilla,
713 E., and Rodrigo, C.: Variabilidad del viento, oleaje y corrientes en la región norte de
714 los fiordos Patagónicos de Chile, *Revista de Biología Marina y Oceanografía*, 46,
715 363-377. . 2011.

716 Mans, C., Bramato, S., Baquerizo, A., and Losada, M.: Surface Seiche Formation on a
717 Shallow Reservoir in Complex Terrain, *J. Hydraul. Eng-Asce*, 137, 517-529, 2011.

718 Maas, L. R. M., and Lam, F.-P. A.: Geometric focusing of internal waves, *J. of Fluid Mech.*,
719 300, 1–41, doi: 10.1017/S0022112095003582, 1995.

720 Monismith, S.: An experimental study of the upwelling response of stratified reservoirs to
721 surface shear stress, *J. of Fluid Mech.*, 171, 407-439, doi:
722 10.1017/S0022112086001507, 1986.

723 Montero, P., Daneri, G., Gonzalez, H., Iriarte, J. L., Tapia, F.J., Lizarraga, L., Sanchez, N.,
724 and Pizarro, O.: Seasonal variability of primary production in a fjord ecosystem of
725 the Chilean Patagonia: Implications for the transfer of carbon within pelagic food
726 webs, *Cont. Shelf Res.*, 31, 202-215, doi: 10.1016/j.csr.2010.09.003, 2011.

727 Mortimer, C. H.: Water movements in lakes during summer stratification; evidence from
728 distribution of temperature in Windermere, *Phil. Trans. Roy. Soc. London*, 236, 355-
729 404, doi : 10.1098/rstb.1952.0005, 1952.

730 Münnich, M., Wuest, A., and Imboden, D. M.: Observations of the 2nd Vertical-Mode of the
731 Internal Seiche in an Alpine Lake, *Limnol. Oceanogr.*, 37, 1705-1719, doi:
732 10.4319/lo.1992.37.8.1705, 1992.

733 Niemeyer, H. & P. Cereceda.: *Hidrografía. Geografía de Chile*, Tomo VIII, Instituto
734 Geográfico Militar, Chile, 320 pp., 1984.

735 Palma, S., and Silva, N.: Distribution of siphonophores, chaetognaths, euphausiids and
736 oceanographic conditions in the fjords and channels of southern Chile, *Deep-Sea Res.*
737 *Pt. II*, 51, 513-53, doi:10.1016/j.dsr2.2004.05.001, 2004.

738 Pantoja, S., Iriarte, J. L., and Daneri, G.: Oceanography of the Chilean Patagonia, *Cont. Shelf*
739 *Res.*, 31, 149-153, doi: 10.1016/j.csr.2010.10.013, 2011.

740 Parsmar, R., and Stigebrandt, A.: Observed damping of barotropic seiches through baroclinic
741 wave drag in the Gullmar Fjord, *J. Phys. Oceanogr.*, 27, 849-857, 1997.

742 Pawlowicz, R.: Observations and linear analysis of sill-generated internal tides and estuarine
743 flow in Haro Strait, *J. Geophys. Res-Oceans*, 107, doi: 10.1029/2000JC000504, 2002.

744 Pickard, G. L.: Some Physical Oceanographic Features of Inlets of Chile, *Journal of the*
745 *Fisheries Research Board of Canada*, 28, 1077-1106, 1971.

746 Rabinovich, A.: Seiches and Harbor Oscillations, in: Handbook of Coastal and Ocean
747 Engineering, Y. Kim (ed.), World Scientific Publishing Co, United States, 193-236,
748 2010.

749

750 Ross L., Pérez-Santos, I., Valle-Levinson, A., Schneider, W.: Semidiurnal internal tides in a
751 Patagonian fjord, *Prog. in Oceanogr.*, 129, 19-34, doi: 10.1016/j.pocean.2014.03.006,
752 2014.

753 Schneider, W., Pérez-Santos, I., Ross, L., Bravo, L., Seguel, R. and Hernández, F.: On the
754 hydrography of Puyuhuapi Channel, Chilean Patagonia. *Prog. in Oceanogr.*, 129, 8–
755 18, doi: doi:10.1016/j.pocean.2014.03.007, 2014.

756 Simpson, J. H., Wiles P. J., and Lincoln, B. J.: Internal seiche modes and bottom boundary-
757 layer dissipation in a temperate lake from acoustic measurements, *Limnol.*
758 *Oceanogr.*, 56, 1893-1906, 2011

759 Stevens, C., Imberger, J.: The initial response of a stratified lake to a surface shear stress, *J.*
760 *of Fluid Mech.*, 312, 39-66, doi: 10.1017/S0022112096001917, 1996.

761 Stigebrandt, A.: Vertical diffusion driven by internal waves in a sill Fjord, *J. Phys. Oceanogr.*
762 6, 486-495, 1976.

763 Stigebrandt, A.: Some aspects of tidal interaction with fjord constrictions, *Estuarine and*
764 *Coastal Marine Science*, 11, 151-166, doi: 10.1016/S0302-3524(80)80038-7, 1980

765 Stigebrandt, A., and Aure, J.: Vertical Mixing in Basin Waters of Fjords, *J. Phys. Oceanogr.*,
766 917-926, 1989.

767 Svendsen, H.: Exchange processes above sill level between fjords and coastal water, in *Fjord*
768 *Oceanography*, H. Freeland, Farmer, D. and Levings C. (eds.), Plenum Press, USA,
769 355-361, 1980.

770 Thompson, R. O. R. Y., and Imberger J.: Response of a numerical model of a stratified lake
771 to a wind stress, in *Proceedings of the 2nd International Symposium on Stratified*
772 *Flows*, Trondheim, Norway, 24-27 June 1980, 562-570, 1980.

773 Thorpe, S.: Near-resonant forcing in a shallow two-layer fluid: a model for the internal surge
774 in Loch New?, *J. of Fluid Mech.*, 63, 509-527, doi: 10.1017/S0022112074001753,
775 1974.

776 Torrence C., and Compo, G.P.: A practical guide to wavelet analysis, *B. Am. Meteorol. Soc.*,
777 79, 61-78, 1998.

778 Valle-Levinson, A., Sarkar, N., Sanay, R., Soto, D., and León, J.: Spatial structure of
779 hydrography and flow in a Chilean fjord, *Estuario Reloncaví, Estuaries and Coasts*,
780 30, 113-126, doi: 10.1007/BF02782972, 2007.

781 Valle-Levinson, A., Blanco, J. L., and Frangópulos, M.: Depth-dependent overtides from
782 internal tide reflection in a glacial fjord, *Estuaries and Coasts*, 30: 127-136, 2007.

783 van der Lee E.M., and Umlauf, L.: Internal wave mixing in the Baltic Sea: Near-inertial
784 waves in the absence of tides, *J. Geophys. Res-Oceans*, 116, C10016, doi:
785 10.1029/2011jc007072, 2011.

786 Watson, E. R.: Movements of the waters of Loch Ness, as indicated by temperature
787 observations, *The Geographical Journal*, 24, 430-437, doi: 10.2307/1775951, 1904.

788 Weddernburn, E. M.: An experimental investigation of the temperature changes occurring in
789 fresh-water lochs, *Proc. R. Soc. Edinb.*, 28, 2-20, doi: 10.1017/S0370164600011524,
790 1907.

791 Weddernburn, E. M. and Young, A.: Temperature observations in Loch Earn. Part II, *Trans.*
792 *R. Soc. Edinb.*, 50, 741-767, doi: 10.1017/S0080456800017026, 1915.

793 Wiegand, R. C., and Chamberlain, V.: Internal waves of the second vertical mode in a
794 stratified lake, *Limnol. Oceanogr.*, 32, 29-42, 1987.
795

796 **Figure captions**

797 **Figure 1:** Study region and location of the measuring stations. Left insert shows the area of
798 the Reloncavi fjord (A). The location of the Reloncavi sound (B) is also shown. The right
799 insert shows the study area (close-up view of A) and the positions of all measurements.
800 Numbers are CTD stations.

801

802 **Figure 2:** Seasonal profiles of density and bathymetry of the region. The upper inserts show
803 the seasonal mean density profiles in each sub-basin of the fjord (a-d). In the insert below
804 (e.), the along-fjord bathymetry and sub-basin nomenclature are shown. The black line
805 represents the mean pycnocline depth, and corresponding standard deviations are represented
806 by the gray shading.

807

808 **Figure 3:** a) Along-fjord wind stress, positive up to the fjord; (b) sealevel, (c) Puelo river
809 discharge, where the straight line represents the long-term mean and contours of along-fjord
810 currents at (d) Cochamo, (e) Puelo and (f) the mouth. In the filled contours, the blue (red)
811 colors indicate a net outflow (inflow).

812

813 **Figure 4:** Spectra of along-fjord currents (above) at the mouth (a), Puelo (b) and Cochamo
814 (c). Here black line indicate the averaged spectra for the upper layer (depths $\leq h_1$) whereas
815 gray lines showed spectra for currents at depths $> h_1$. (d) sealevel spectra at the mouth (black
816 line) and at Cochamo (gray). (e) wind stress spectra for their along-fjord (black) and cross-
817 fjord (gray) components. At the bottom each panel the 95% of confidence intervals for 48, 24
818 and 12 degrees of freedom are shown.

819

820 **Figure 5:** The left insert shows mean density (σ_t) within the sub-basins. The pannels to the
821 right of these show the first 3 baroclinic $\psi_n(z)$ modes and modal speeds obtained from the
822 CSM analysis (normalized). Note that phase velocity is in [m s⁻¹].

823

824 **Figure 6.** Band-passed along-fjord currents. Contours of band-passed (70-90 h) along-fjord
825 currents. Negative (positive) currents in blue (in red) imply an outflow (inflow). Note the
826 dotted square at the middle of August it is zooming on figure 9.

827

828 **Figure 7.** Projected along-fjord currents and kinetic energy (K_E). Here presented the 1 to 3
829 modal projections of the along-fjord band-passed (60-100 h) currents at the mouth. At the
830 bottom, present the K_E estimated using the components projected using modes 1-3 (black),
831 the 3 days band-pass (red), and the diurnal and semi-diurnal band-pass currents (blue).

832

833 **Figure 8.** Coherence and phase wavelet spectra. Time series of along fjord wind-stress (a),
834 and coherence and phase wavelet spectra for the relation mouth/Puelo (b, c) and
835 Puelo/Cochamo (d, e). In the contours, the thick black line indicates squared coherence ≥ 0.6 ,
836 only the associated phases were present on the phase wavelet. The thick black curve is the
837 influence cone for the wavelet estimations.

838

839 **Figure 9.** Time-series of along-fjord wind stress (τ) and contours of along-fjord Currents and
840 Temperatures at Cochamo, Puelo and the mouth. There are three states of wind stress based
841 on the Wedderburn number (W) with (a) strong $W < 1$, (b) weak $W > 1$ and moderate $W \sim 1$
842 winds. Note that contours of the Currents and Temperature for a given location are plotted
843 together. The arrows represent the 3 days band-pass vertical velocities where the maximum
844 was 1 cm s^{-1} .

845

846 **Figure 10.** Damping signal in currents. During a period of weak winds ($W > 1$) at Cochamo
847 (16 to 24 August 2008). The band-pass currents at the 3m depth (black line) was compared
848 with a damping oscillatory curve $x(t) = A e^{(-kt)} \cos(\omega t + \phi)$ (gray line). The damping time (T_d)
849 was 3.6 times longer than the fundamental internal period (T_N).

850

851

852

853

854

855

856

857 **Table titles**

858

859 **Table 1:** Characteristic of Reloncavi fjord. The name, mean depth (H) and length (L) of each
860 sub-basin and for the entire fjord are presented.

861

862 **Table 2:** Seasonal statistics of the descriptive parameters of the fjord. Here we present the
863 mean depth of the upper layer (h_1), and densities of the upper (ρ_1) and deep layers (ρ_2). In
864 addition, the phase and modal velocities (c) and theirs periods (T) estimated using the
865 Reduced Gravity and Continuously Stratified models are shown.

866

867 **Table 1.**

Sub-basin	Description	H [m]	L [km]
I	mouth–Marimeli	440	14.0
II	Marimeli – Puelo	250	13.0
III	Puelo–Cochamo	200	17.5
IV	Cochamo–head	82	10.5
Total	mouth -head	250	55

868

869

870

871

872

873

874

875

876

877

878

1 **Table 2.**

2

Reduced Gravity Model (RGM)					
	h_1 [m]	ρ_1 [kg m ⁻³]	ρ_2 [kg m ⁻³]	c [m s ⁻¹]	T [days]
Winter	4.60 ± 0.60	1009.72± 4.32	1024.62 ± 0.74	0.76 ± 0.01	3.37 ± 0.03
Spring	4.79 ± 0.53	1007.63± 5.32	1024.78 ± 0.62	0.87 ± 0.02	2.92 ± 0.03
Summer	4.68 ± 0.26	1008.77± 3.26	1024.78 ± 0.63	0.83 ± 0.01	3.07 ± 0.02
Autumn	4.05 ± 0.41	1009.90± 3.92	1024.95 ± 0.48	0.75 ± 0.01	3.38 ± 0.03

Continuous Stratified Model (CSM)						
	c_1 [m s ⁻¹]	c_2 [m s ⁻¹]	c_3 [m s ⁻¹]	T_1 [days]	T_2 [days]	T_3 [days]
Winter	0.73 ± 0.11	1.46 ± 0.21	2.18 ± 0.32	3.50 ± 0.25	1.75 ± 0.13	1.17 ± 0.08
Spring	0.87 ± 0.10	1.73 ± 0.21	2.59 ± 0.31	2.94 ± 0.18	1.47 ± 0.09	0.98 ± 0.06
Summer	0.84 ± 0.07	1.68 ± 0.13	2.52 ± 0.20	3.03 ± 0.12	1.51 ± 0.06	1.01 ± 0.04
Autumn	0.77 ± 0.08	1.54 ± 0.15	2.32 ± 0.23	3.30 ± 0.16	1.65 ± 0.08	1.10 ± 0.05

3

4

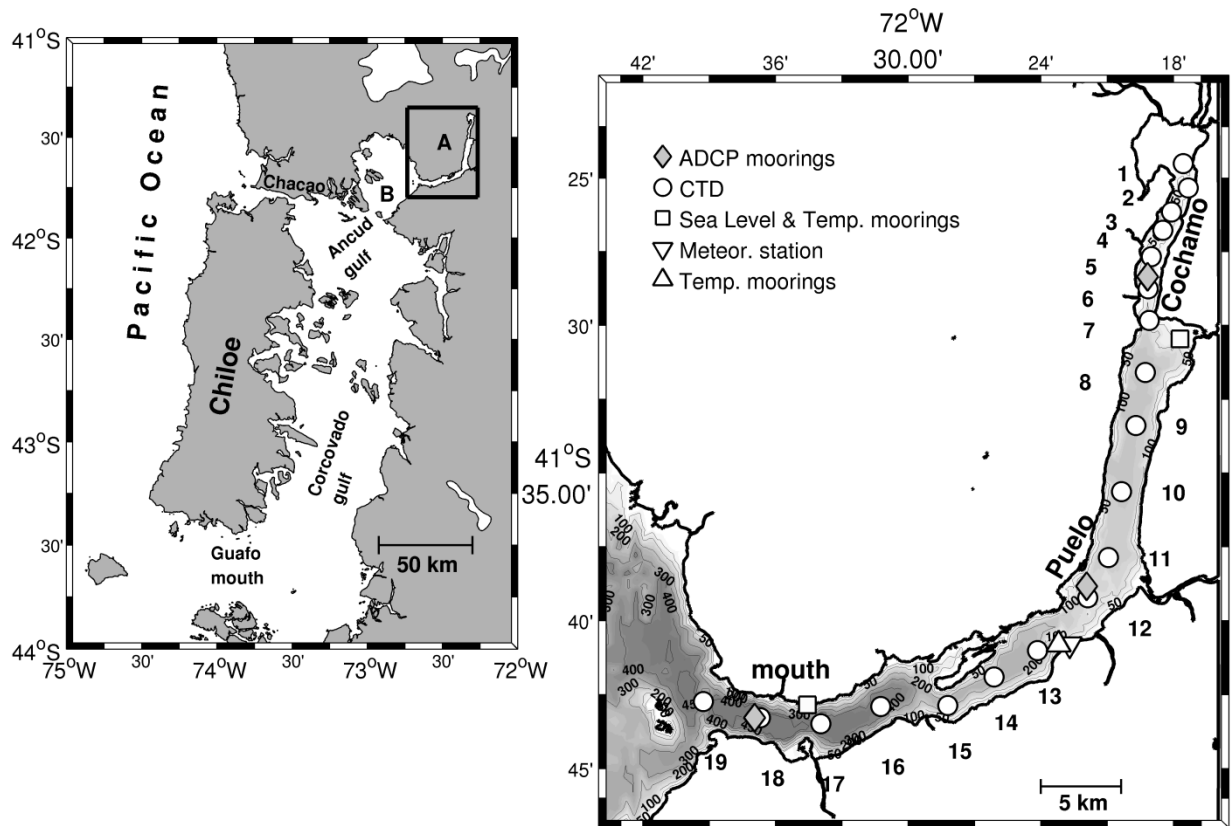


Figure 1: Study region and location of the measuring stations. Left insert shows the area of the Reloncavi fjord (A). The location of the Reloncavi sound (B) is also shown. The right insert shows the study area (close-up view of A) and the positions of all measurements. Numbers are CTD stations.

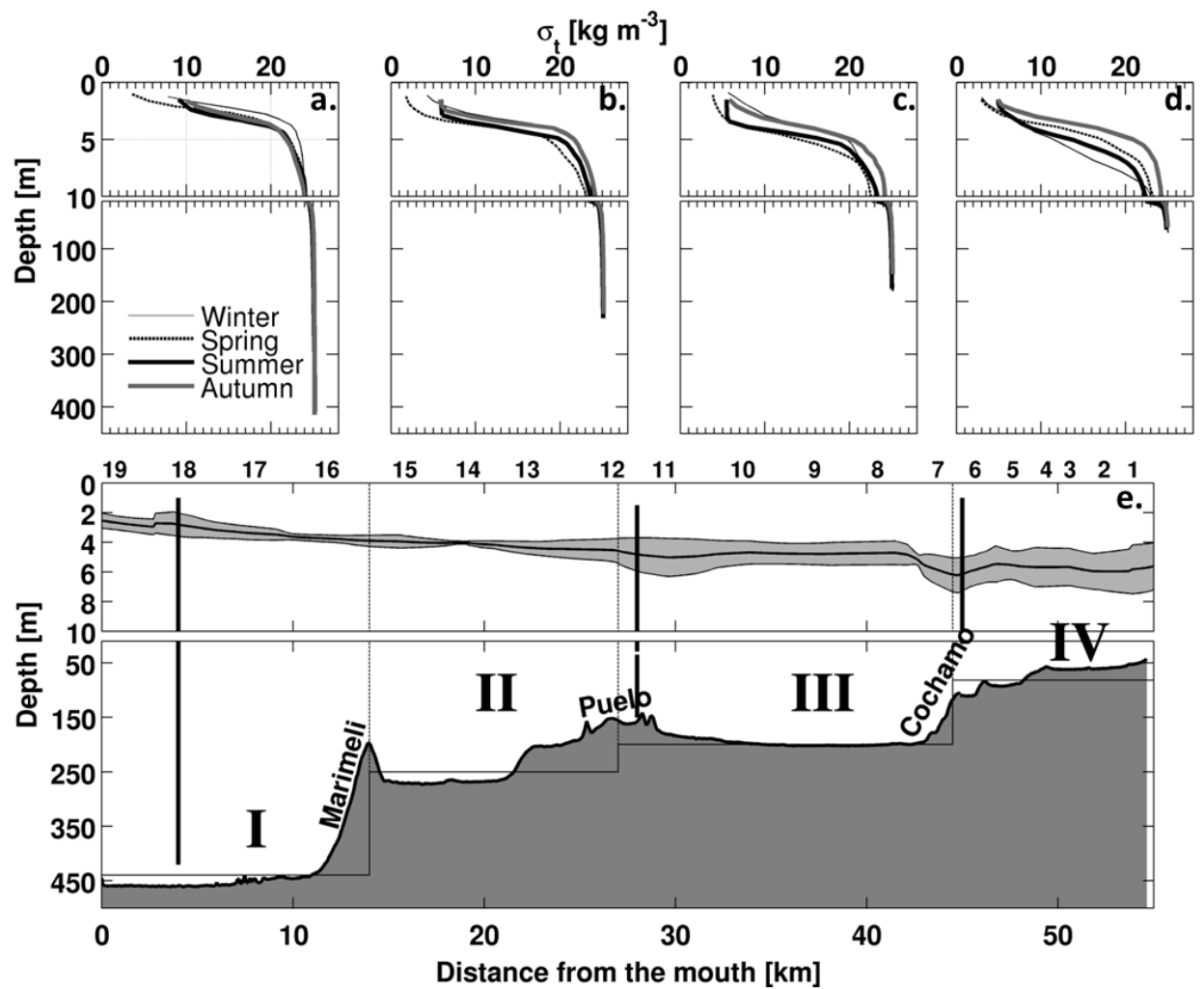


Figure 2: Seasonal profiles of density and bathymetry of the region. The upper inserts show the seasonal mean density profiles in each sub-basin of the fjord (a-d). In the insert below (e.), the along-fjord bathymetry and sub-basin nomenclature are shown. The black line represents the mean pycnocline depth, and corresponding standard deviations are represented by the gray shading.

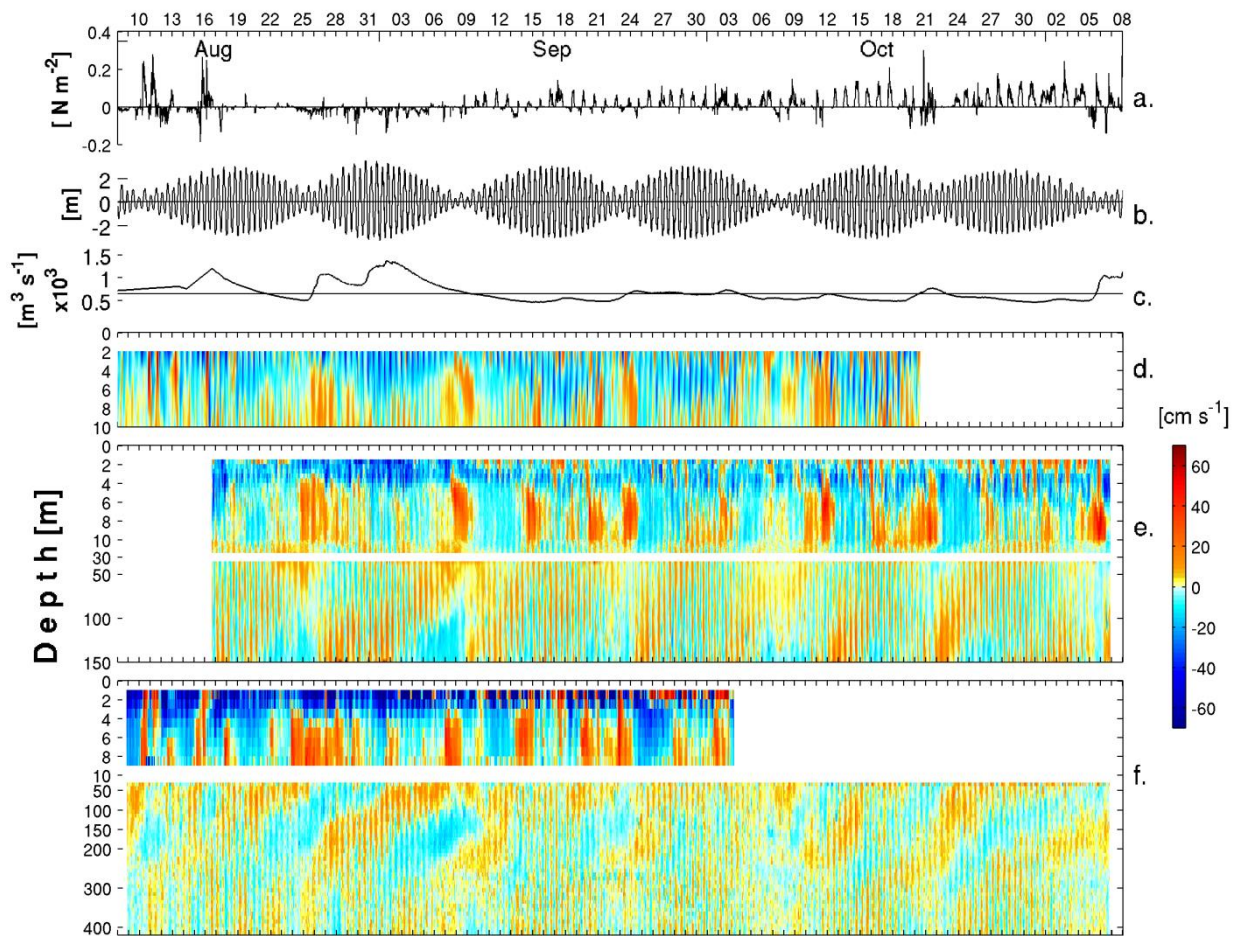


Figure 3: a) Along-fjord wind stress, positive up to the fjord; (b) sealevel, (c) Puelo river discharge, where the straight line represents the long-term mean and contours of along-fjord currents at (d) Cochamo, (e) Puelo and (f) the mouth. In the filled contours, the blue (red) colors indicate a net outflow (inflow).

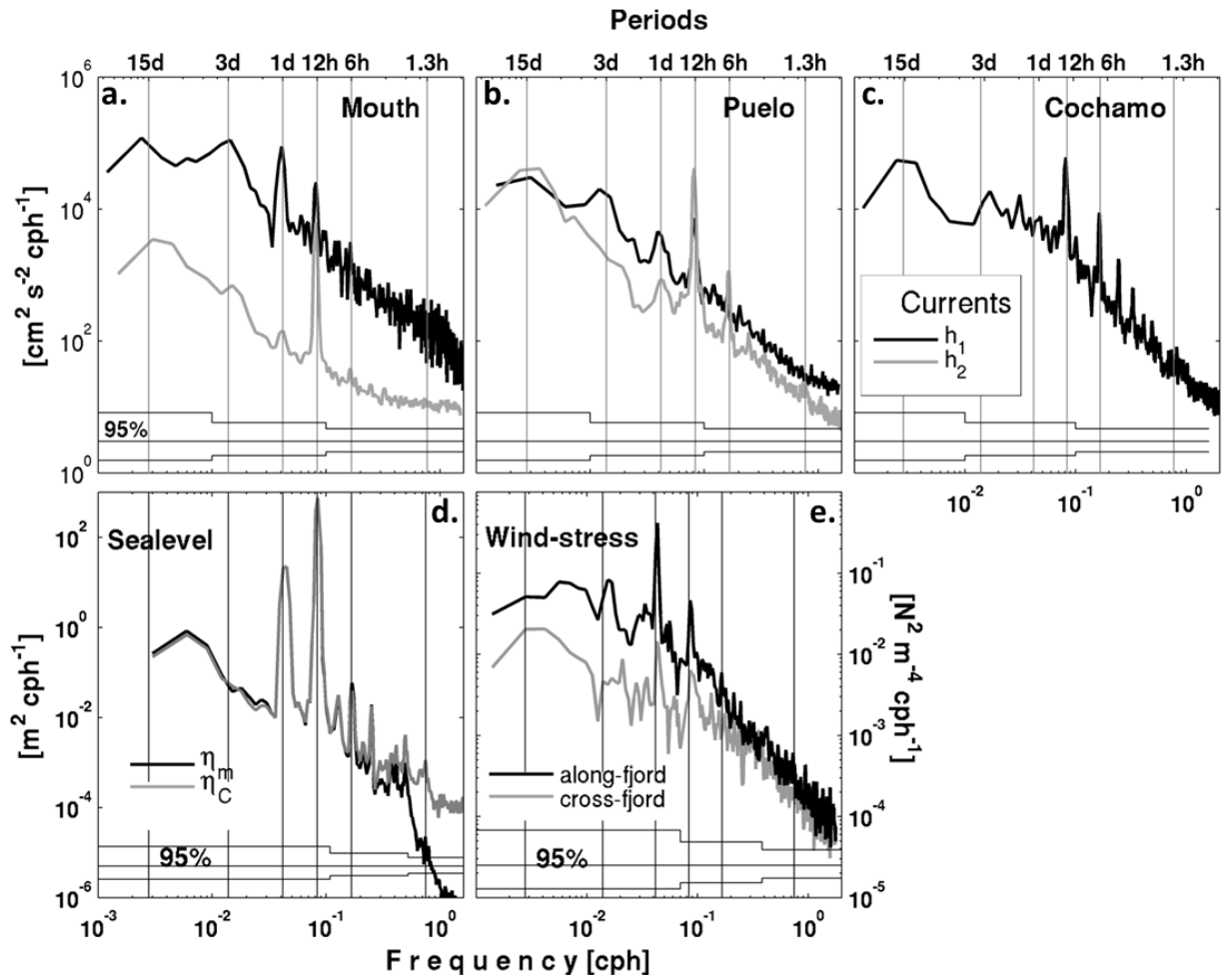


Figure 4: Spectra of along-fjord currents (above) at the mouth (a), Puelo (b) and Cochamo (c). Here black line indicate the averaged spectra for the upper layer (depths $\leq h_1$) whereas gray lines showed spectra for currents at depths $> h_1$. (d) sealevel spectra at the mouth (black line) and at Cochamo (gray). (e) wind stress spectra for their along-fjord (black) and cross-fjord (gray) components. At the bottom each panel the 95% of confidence intervals for 48, 24 and 12 degrees of freedom are shown.

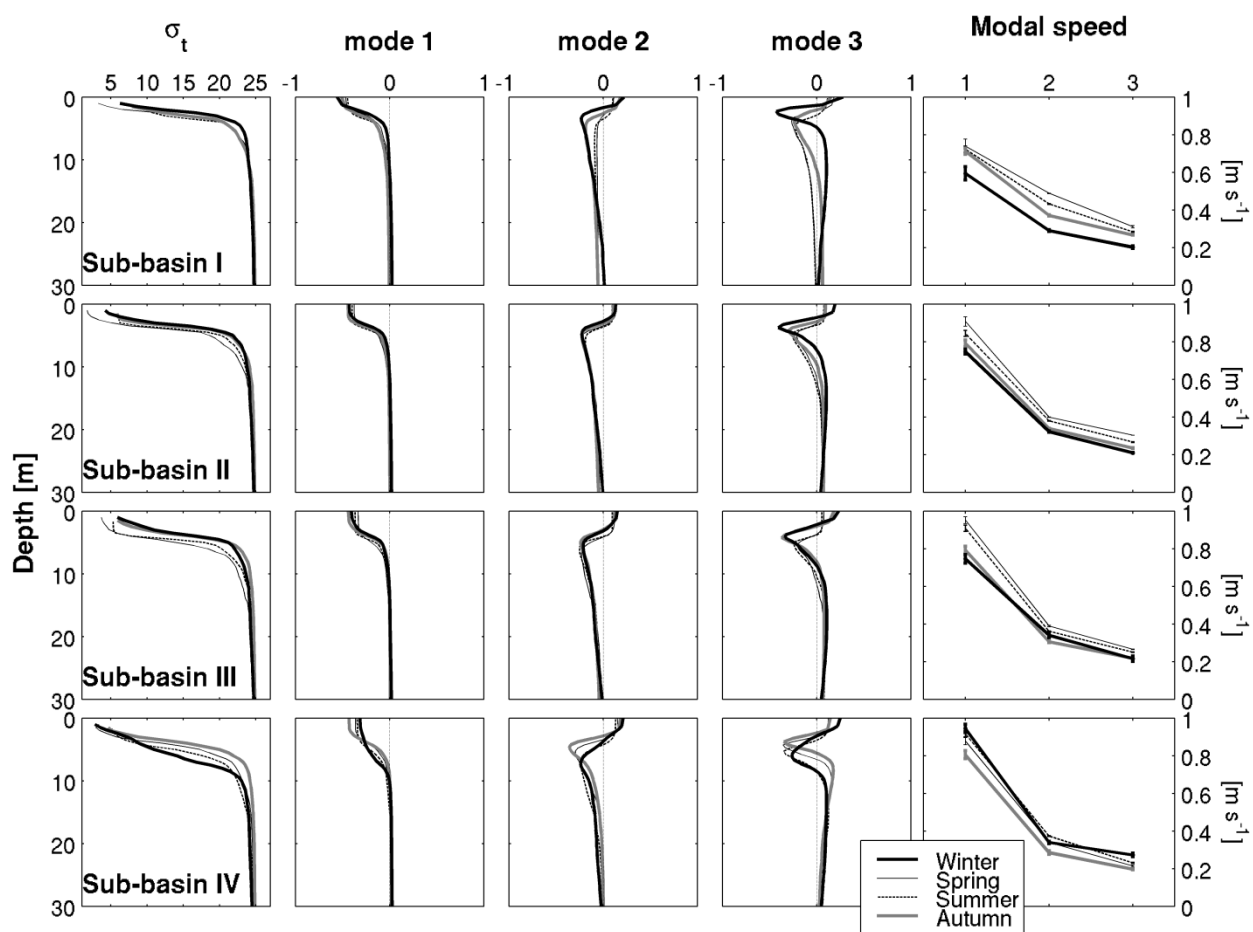


Figure 5: The left insert shows mean density (σ_t) within the sub-basins. The panels to the right of these show the first 3 baroclinic $\psi_n(z)$ modes and modal speeds obtained from the CSM analysis (normalized). Note that phase velocity is in [m s⁻¹].

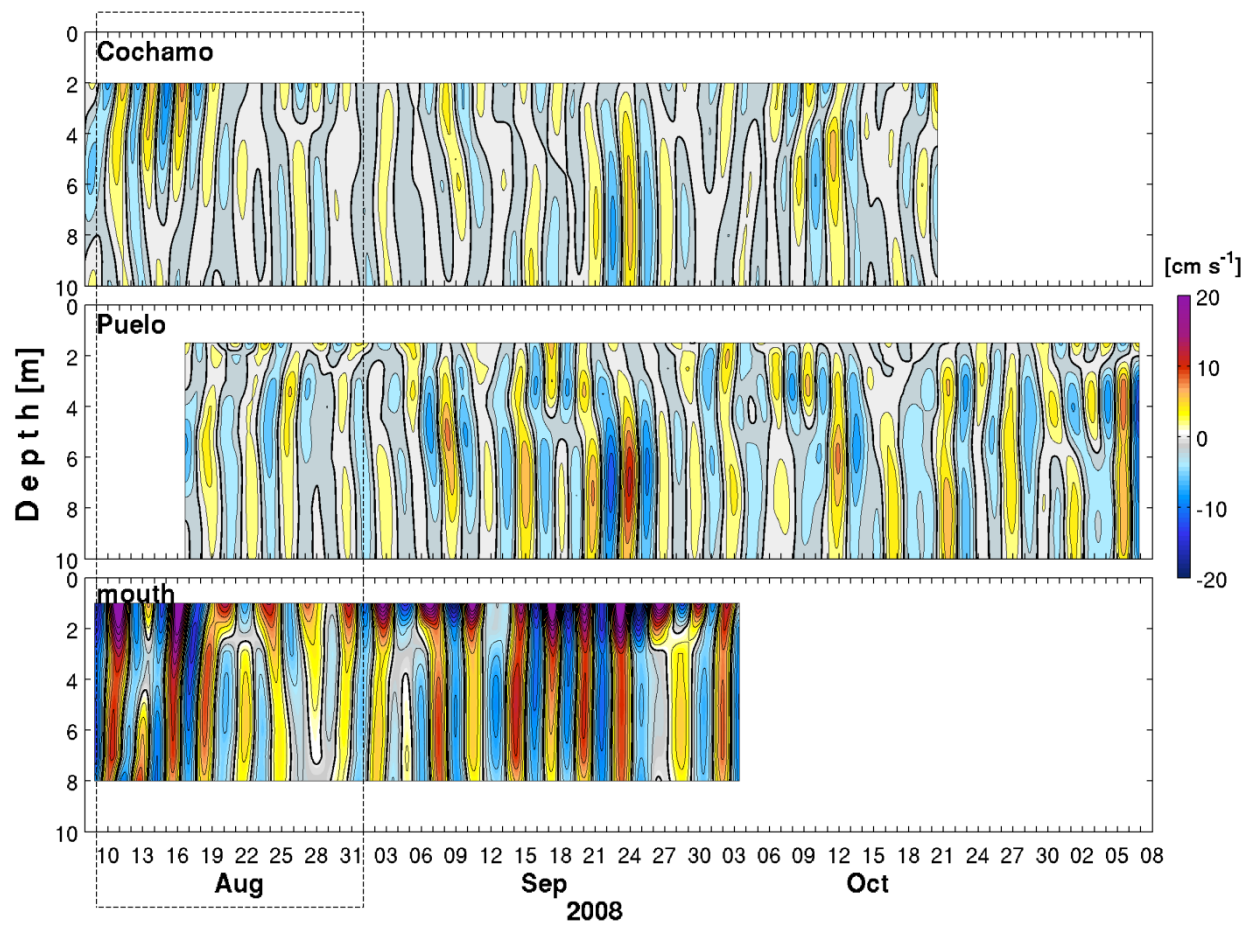


Figure 6. Band-passed along-fjord currents. Contours of band-passed (70-90 h) along-fjord currents. Negative (positive) currents in blue (in red) imply an outflow (inflow). Note the dotted square at the middle of August it is zooming on figure 9.

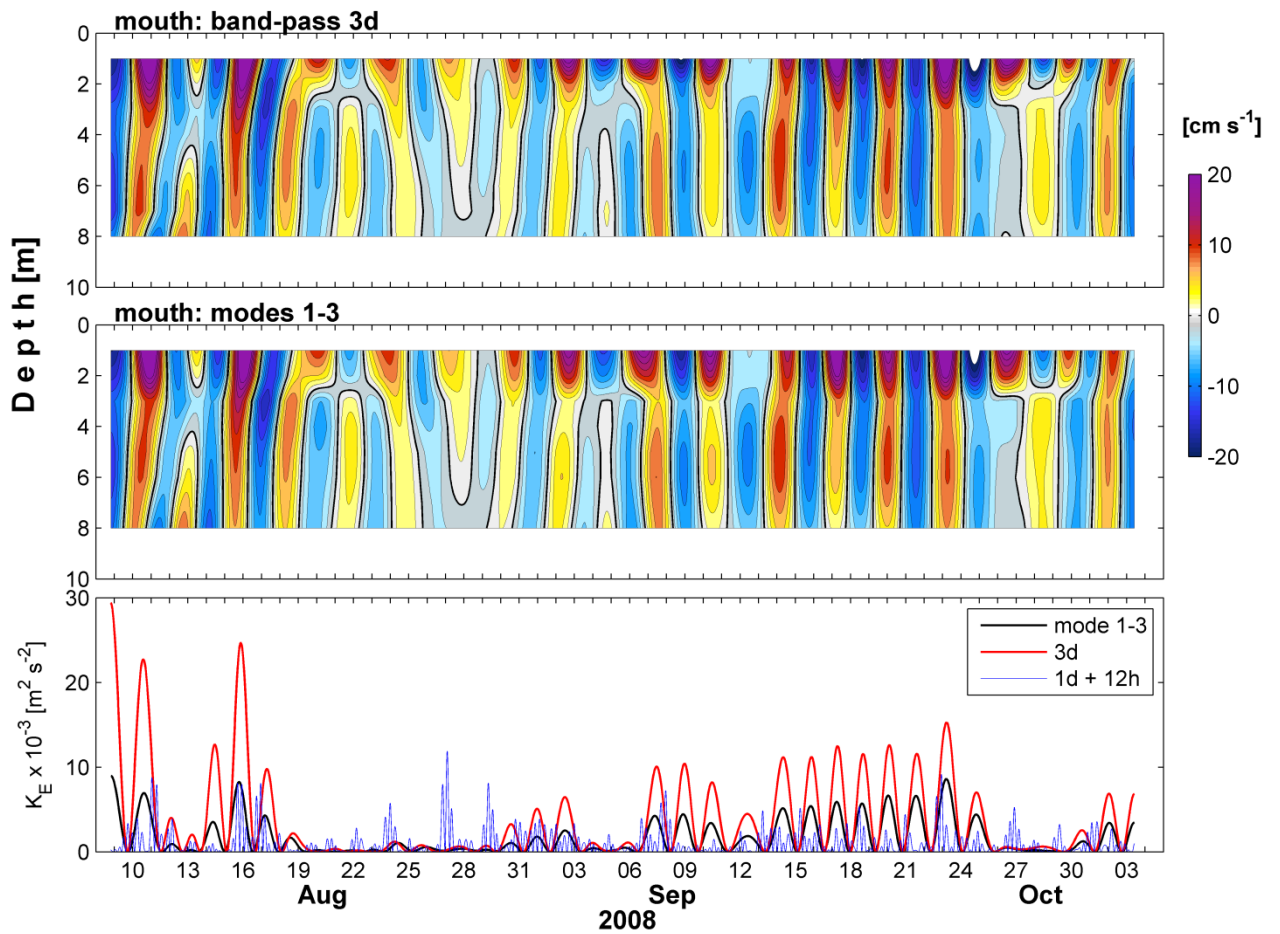


Figure 7. Projected along-fjord currents and kinetic energy (K_E). Here presented the 1 to 3 modal projections of the along-fjord band-passed (60-100 h) currents at the mouth. At the bottom, present the K_E estimated using the components projected using modes 1-3 (black), the 3 days band-pass (red), and the diurnal and semi-diurnal band-pass currents (blue).

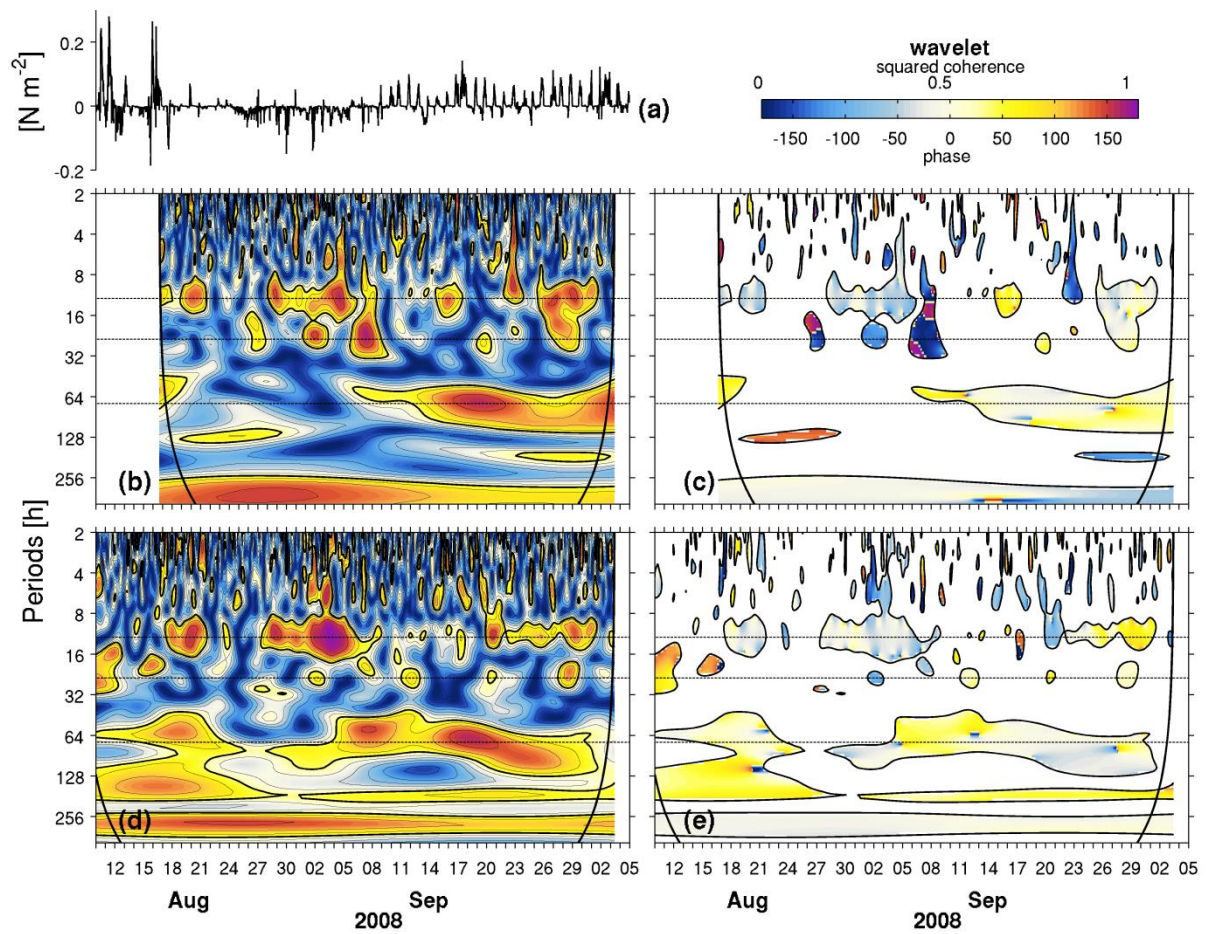


Figure 8. Coherence and phase wavelet spectra. Time series of along fjord wind-stress (a), and coherence and phase wavelet spectra for the relation mouth/Puelo (b, c) and Puelo/Cochamo (d, e). In the contours, the thick black line indicates squared coherence ≥ 0.6 , only the associated phases were present on the phase wavelet. The thick black curve is the influence cone for the wavelet estimations.

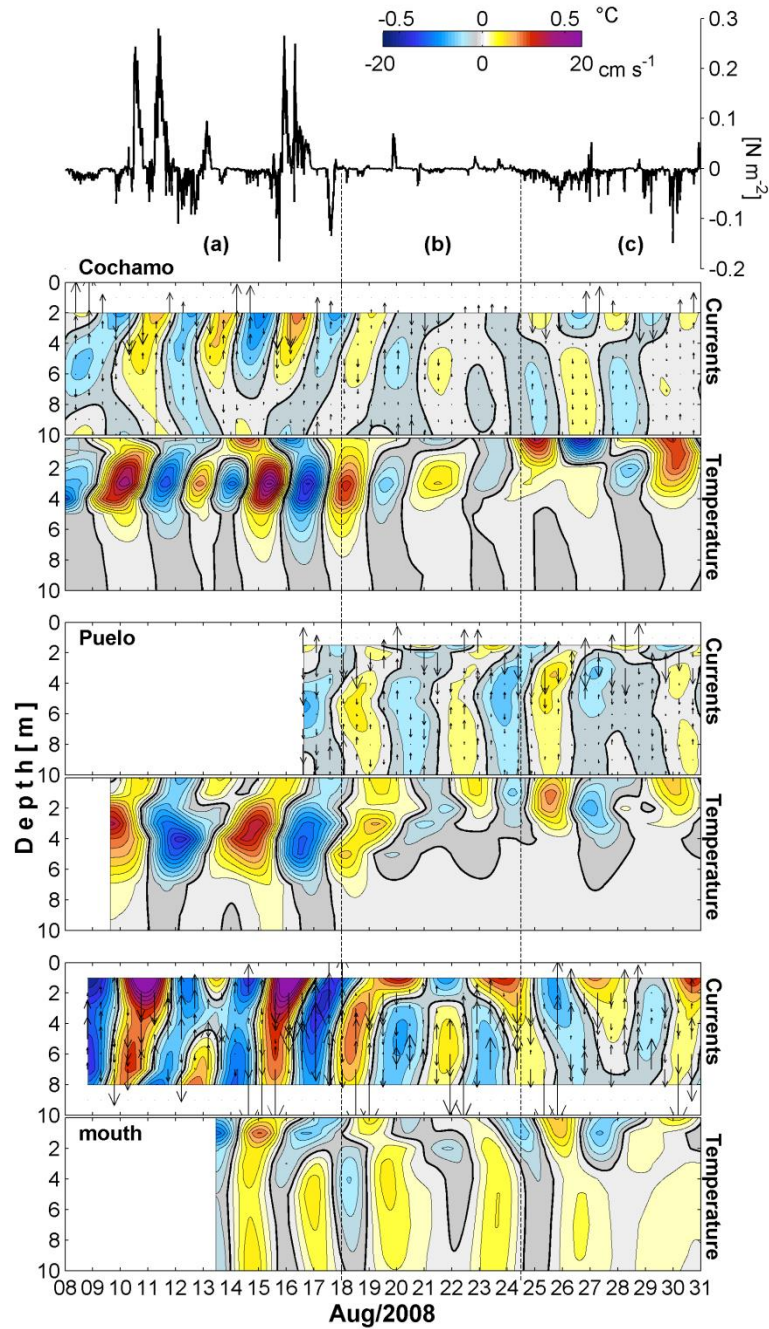


Figure 9. Time-series of along-fjord wind stress (τ) and contours of along-fjord Currents and Temperatures at Cochamo, Puelo and the mouth. There are three states of wind stress based on the Wedderburn number (W) with (a) strong $W < 1$, (b) weak $W > 1$ and moderate $W \sim 1$ winds. Note that contours of the Currents and Temperature for a given location are plotted together. The arrows represent the 3 days band-pass vertical velocities where the maximum was 1 cm s^{-1} .

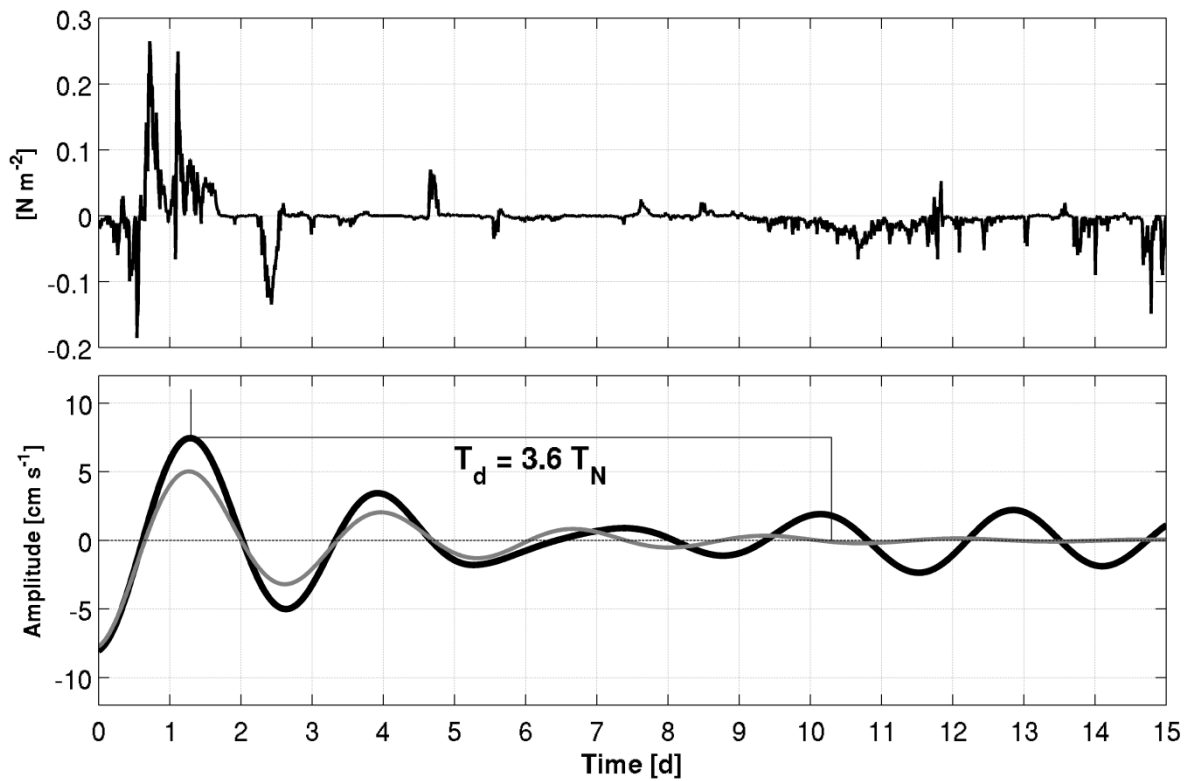


Figure 10. Damping signal in currents. During a period of weak winds ($W > 1$) at Cochamo (16 to 24 August 2008). The band-pass currents at the 3m depth (black line) was compared with a damping oscillatory curve $x(t) = A e^{(-kt)} \cos(\omega t + \phi)$ (gray line). The damping time (T_d) was 3.6 times longer than the fundamental internal period (T_N).